



Micro-electricity generation using solar thermal design and modelling thermosiphon applications from waste recycled materials

T.J. Abodunrin^{*}, C.J. Ofulue

Physics Department, Covenant University, Canaanland, Ota, Ogun State, Nigeria

ABSTRACT

In this study, the abundant heat energy available from daily insolation in tropical climates is converted into DC current via a reversible thermoelectric effect. Recyclable components were employed in the construction of a simple solar-thermoelectric generator. The design used is based on the power tower method (without heliostats) of generating electricity from a steam-powered turbine. Recyclable waste materials such as soda can, insulation, support stand, (bottle tops) and plane mirrors were used. Integration of this TEG into a cogeneration system produced average steam temperature of 60 °C in 330 s, from concentrated Solar Power (CSP) from 720 plane mirrors over a land area of 4 m². Steam emanating from the boiler was used to turn eight light weight bottle tops affixed to a rotor, under standard conditions of air mass of 1 atm. The thermo-electrical performance was determined from Z, figure of merit. Given that the electrical conductivity (σ), thermal conductivity (λ) and Seebeck coefficient of the thermo-power (S) of all materials used were assumed to be constant. The output energy directed through wires to a step-up transformer, generated an electromotive force which adequately lighted a 1.2 V light emitting diode.

1. Introduction

The history of solar thermal systems dates back to the late 19th century, with French scientist Augustin Mouchot [1]. Since then, there has been diverse applications of solar thermal energy ranging from steam engines powered by steam produced from sunlight, Liquid fuel engines, concentrators and war-time security [2–6]. This direct application of solar energy can be classified under three types namely, low-temperature, medium-temperature and high temperature solar heating systems. Some systems are passive, while others are active requiring other external energy to function. Dual purpose solar thermal systems function as both collectors and heat storage either short-term or inter-seasonal; and distribution within a structure or a district heating network. In higher-order concentrators, where the reflectors or lenses are stationary, a tracker is incorporated to accentuate the focus of the reflectors or lenses necessary to generate sufficient power [7–10]. A tracking system always increases the cost and complexity of any plant. Although heating is the most obvious application of solar thermal installations, addressing practical side effects of high efficiencies is pertinent. Reduction of plant's collector size, total land use per unit power generated, and reducing the environmental impacts of a power plant as well as its expense are extended solutions that guarantee the sustainability of renewable energies.

Amongst the variety of solar system designs, the technique employed differs, parabolic troughs power plants use a curved mirrored trough, in

which the receiver may be enclosed in a glass vacuum chamber which significantly reduces convective heat loss. The limitation is that, only about 15% overall efficiency from the collector to the main power grid is recorded [11]. Lightweight mirrors are features which enable single-axis tracking system sunlight focus onto a network of stationary steel pipes. In addition, enclosure shelters the mirrors from adverse conditions such as, wind, extreme temperatures, rain, dust and humidity. This allows them to achieve higher temperature rates and increased performance [12]. In Power or central tower power plants, capture and focus of solar thermal energy is accomplished with heliostats occupying a large area. Concentrated radiation is used to heat up a fluid which is usually molten salt, inside the receiver. The major advantage this design has over the parabolic trough is that higher temperature is achieved due to thermal efficiency retention. Thus, thermal energy is cheaper, stored for later use in evenings and can be converted to electricity more efficiently [13].

A Dish Stirling system uses a large, reflective, parabolic dish similar to a satellite dish comprising of several, smaller reflective mirrors. These components introduce a torque which can be converted to electricity using an electric generator. Its output of about 30% ranks the highest efficiency of solar radiation energy from among all known solar technologies. In terms of cost saving, linear Fresnel reflector power plant uses single-axis tracking with series of flat structurally simple mirrors to focus light onto one or more linear receivers positioned above mirrors [14].

The efficiency of heat engines, dry heat exchangers increase with the

^{*} Corresponding author.

E-mail address: temitope.abodunrin@covenantuniversity.edu.ng (T.J. Abodunrin).



Fig. 1. Cross-section of STEG set-up.

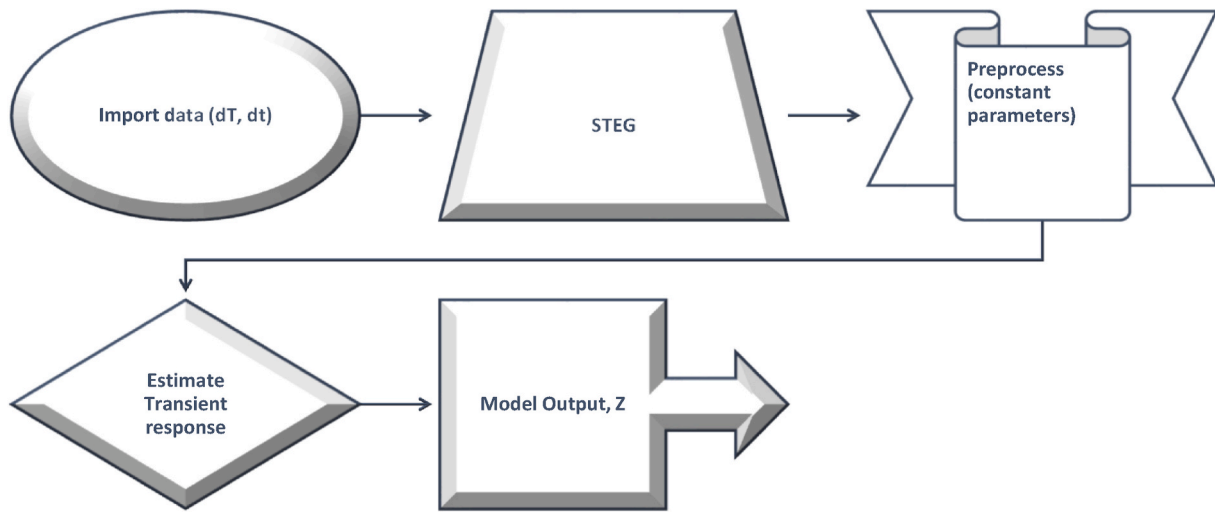


Fig. 2. STEG cogeneration system.

Table 1
Day1 Vs Day 2 readings.

Day 1				Day 2			
Time (h)	Dist. (cm)	Ht. (cm)	Tempt. (°C)	Time (h)	Dist. (cm)	Ht. (cm)	Tempt. (°C)
11:30	50.0	38.0	35.0	11:30	49.2	45.0	25.0
12:00	58.0	38.0	59.0	12:00	80.1	45.0	44.0
12:30	67.2	37.5	84.0	12:30	68.5	34.0	79.0
13:00	89.3	37.2	90.0	13:00	76.0	34.5	94.0
13:30	56.4	39.0	95.0	13:30	61.0	41.0	98.0
14:00	55.2	44.0	97.0	14:00	46.5	46.5	79.0
14:30	42.0	51.5	75.0	14:30	32.0	53.0	62.0
15:00	38.5	63.0	50.0	15:00	32.0	65.7	40.0

Table 2
Day 3 Vs Day 4 readings.

Day 3				Day 4			
Time (h)	Dist. (cm)	Ht. (cm)	Tempt. (°C)	Time (h)	Dist. (cm)	Ht. (cm)	Tempt. (°C)
11:30	-	-	-	11:30	50.0	44.5	30.0
12:00	-	-	-	12:00	59.2	44.5	50.0
12:30	-	-	-	12:30	64.2	39.7	46.0
13:00	-	-	-	13:00	-	-	-
13:30	60.0	45.0	60.0	13:30	-	-	-
14:00	50.0	55.7	44.0	14:00	-	-	-
14:30	48.2	59.7	40.0	14:30	-	-	-
15:00	43.1	61.0	32.0	15:00	-	-	-

Table 3
Day vs day 6 readings.

Day 5				Day 6			
Time (h)	Dist. (cm)	Ht. (cm)	Tempt. (°C)	Time (h)	Dist. (cm)	Ht. (cm)	Tempt. (°C)
11:30	50.0	44.5	30.0	11:30	59.2	44.5	32.0
12:00	57.4	44.5	60.0	12:00	66.0	40.2	67.0
12:30	65.0	39.7	73.0	13:00	83.0	37.0	80.0
13:00	84.4	36.5	84.0	13:30	72.4	41.5	89.0
13:30	73.7	40.0	90.0	14:00	53.1	44.5	77.0
14:00	53.1	45.1	60.0	14:30	45.0	49.5	69.0
14:30	44.0	52.0	70.0	15:00	41.5	64.0	47.0
15:00	40.5	65.7	45.0				

The dashed lines represent unfavorable weather such as rainfall, drizzle and cloud cover.

temperature of the heat source, the latter reduces the plant's water use, an essential feature in the deserts where large solar plants are practical. As temperature increases, different forms of conversion become practical [15].

In circumstances where temperatures below about 95 °C are required, flat plate collectors are used as they do not require temperatures above 200 °C. Even when the heat transfer fluid is stagnant, such temperatures are too low for efficient conversion to electricity. Generally, for temperature reaching 600 °C in steam turbines, efficiency up to 41% have been recorded. Above this temperature, gas turbines are seen to be even more efficient, like between 700 °C and 800 °C. Utilizing

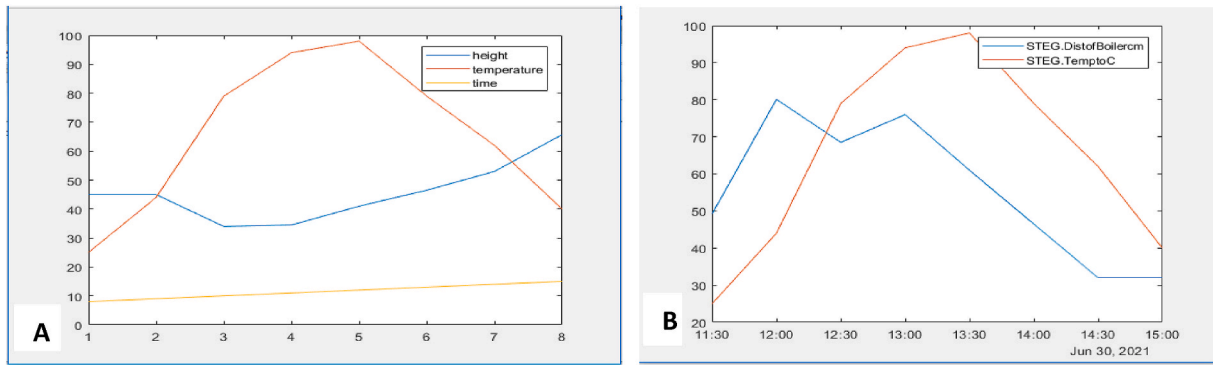


Fig. 3. Comparison of height and distance of boiler with temperature on Day 1.

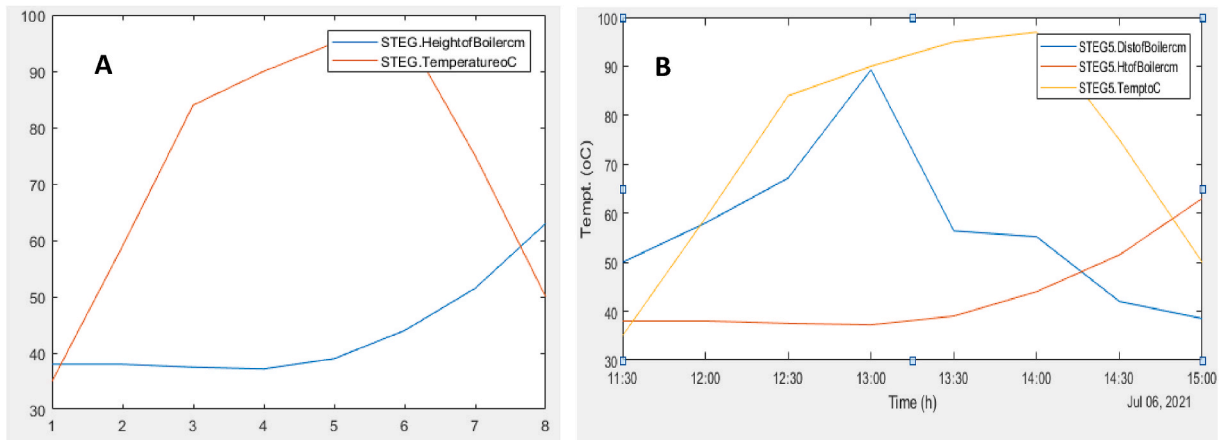


Fig. 4. Comparison of Day 1 and Day 2 heights and distances relative to temperature.

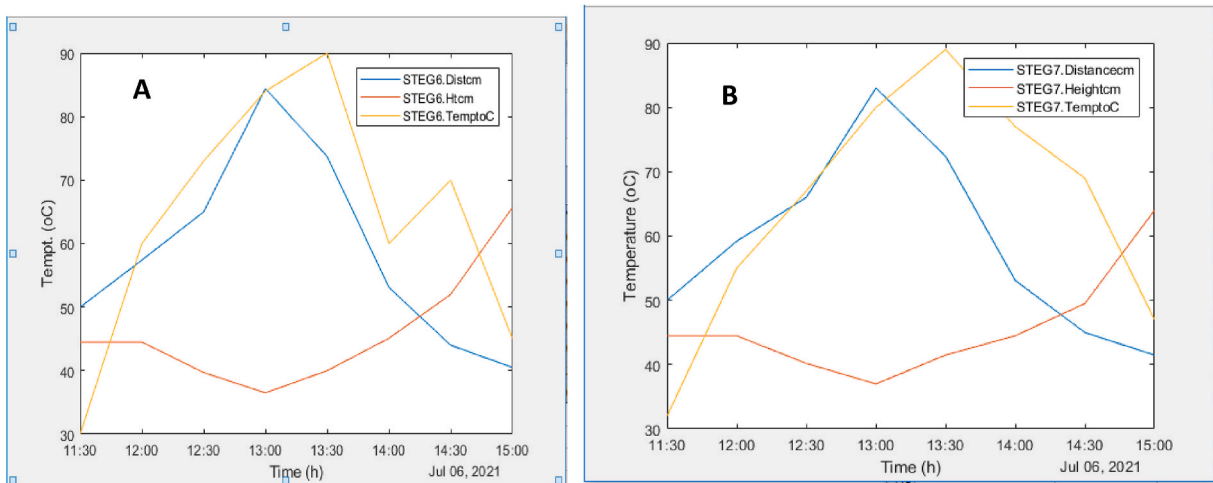


Fig. 5. Comparison of Day 3 and Day 4 heights and distances relative to temperature.

multi-stage turbine systems, salt solutions and different techniques has achieved 50% or more efficiency increase [16]. Another positive development is in the use of high-temperature dry heat exchangers for thermal exhaust, thereby reducing the plant’s water use. This is especially applicable in the deserts where high temperatures also make heat storage more efficient, yielding more solar watt-hours storage per unit of fluid [17].

In practice, collectors are being used to produce approximately 50% with a higher possibility of more hot water required for residential and

commercial use. Figures reveal that, sum total of this provides less than a tenth of the amount expended on energy budgets in economy where electricity is generated from fossil reserves [18]. Temperate climates require a greater collector area but with thermo-siphon installations which have negligible maintenance costs, a further reduction of a household operating costs by \$6 per person per month is possible. Solar water heating can reduce CO₂ emissions of a family of four by 1 ton/year conveniently replacing natural gas or 3 tons/year in replacing electricity [19]. In recent times, temperature gradient is employed in generating

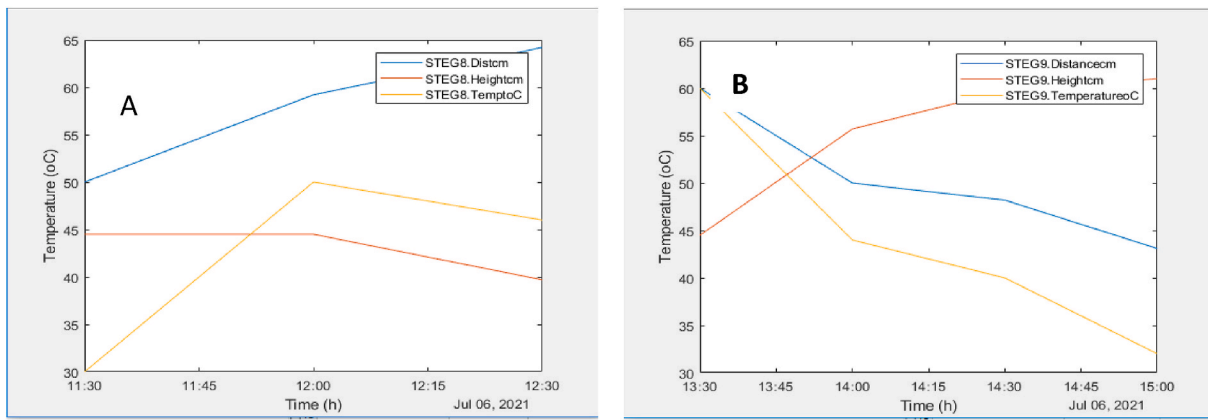


Fig. 6. Comparison of Day 5 and Day 6 heights and distances relative to temperature.

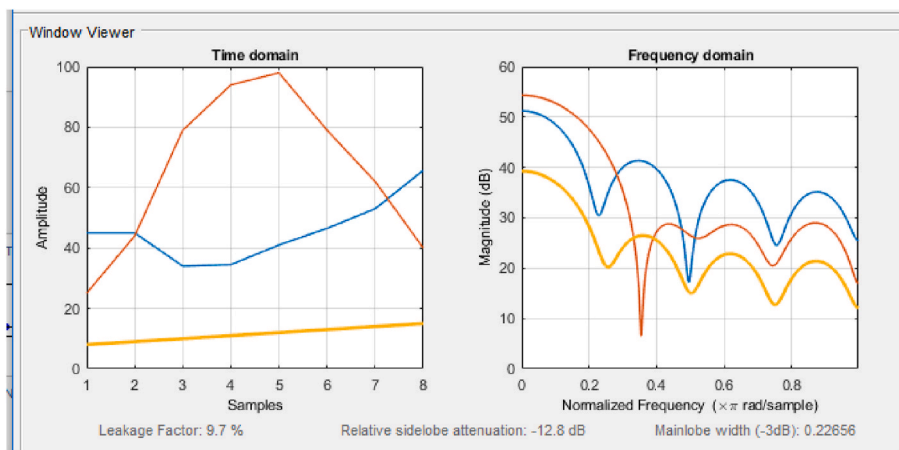


Fig. 7. MATLAB processing of isotherms within a common reference frame.

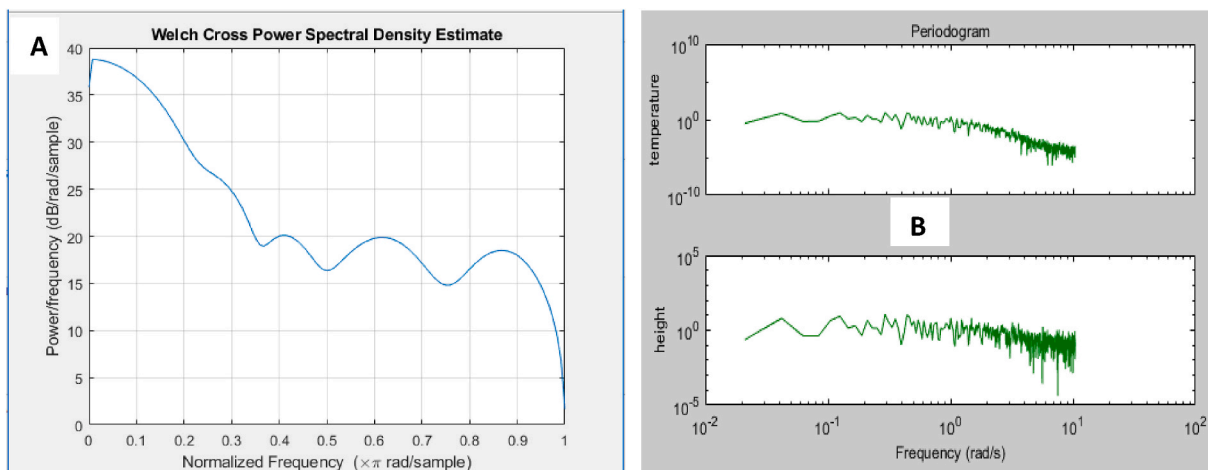


Fig. 8. Illustrates: (a) the spectral density and periodogram of the heat in boiler.

electricity from materials, the material properties determine the electricity produced for any temperature difference. Certain topological materials have been nanostructured and synthesized into proficient thermoelectric devices, using charge transport along mean free path of grain boundaries. In this work, power is generated from waste heat using waste materials and converted into voltage utilizing temperature gradient across a blackbody [20–23].

2. Methodology

This simple design used an array of 720 plain mirrors of dimension 2" X 2" arranged on 6 panels containing 120 units in a matrix of 20 × 6 each. These six modules arranged in an 'H' to optimize and converge solar energy onto a black coated aluminum soda can containing water. The container was suspended from a variable support to represent the power tower method. As the water heats up under standard conditions of

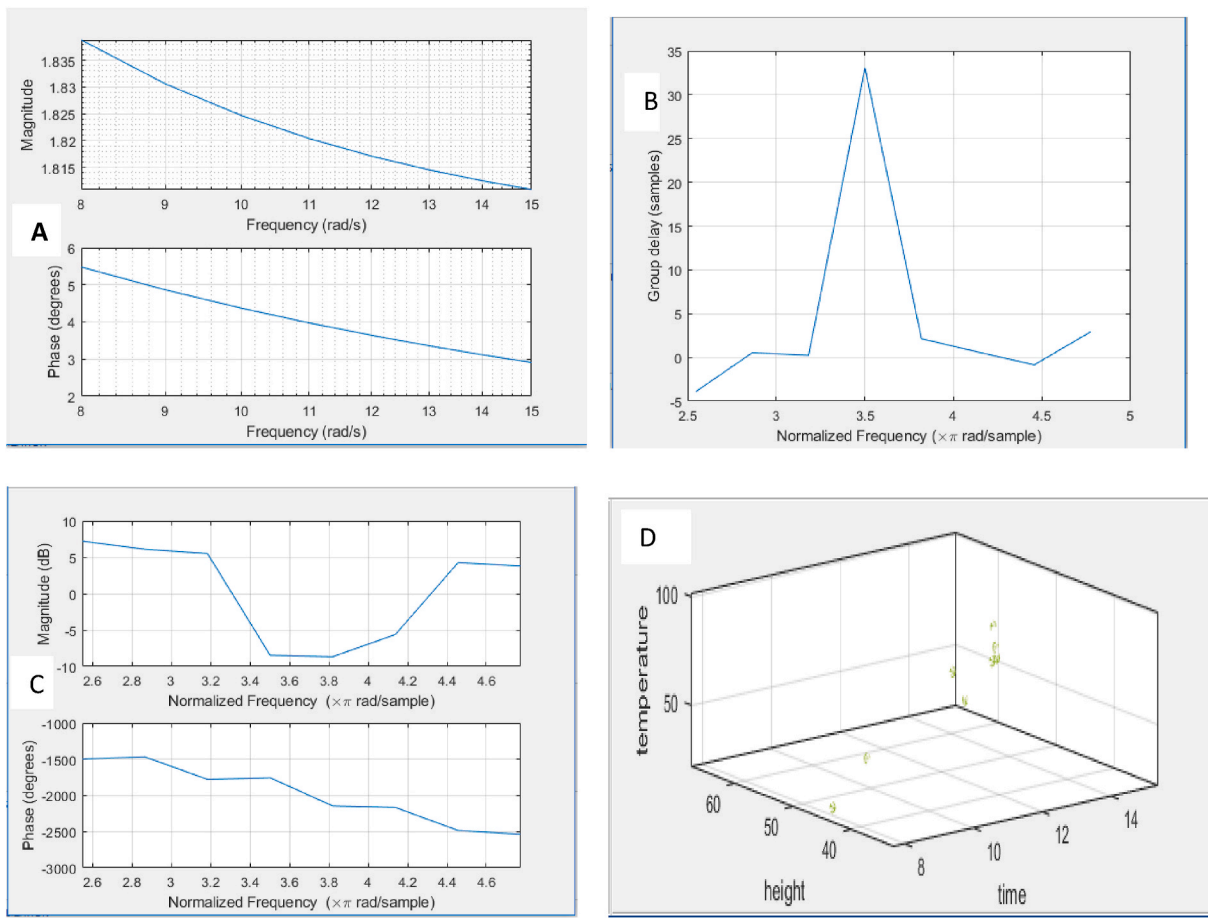


Fig. 9. Illustration of effect of magnitude and phase angle on group delay of steam in STEG.

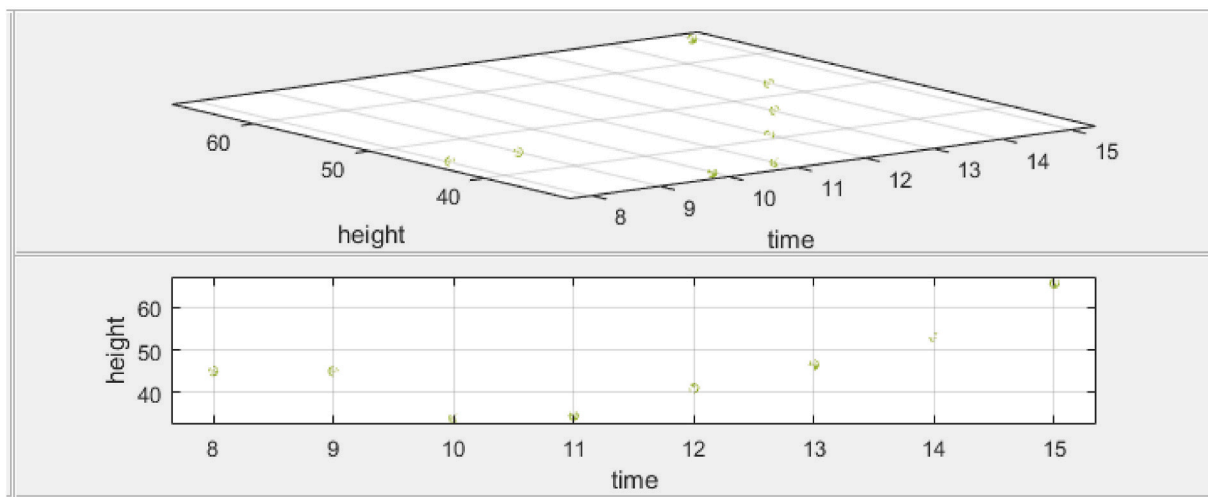


Fig. 10. Aerial View of Contour Vs Residual Stress of steam on turbine.

1 atm air mass, steam generated propelled a turbine made of 8 light weight bottle tops, which was in turn connected to a step-up transformer. The quantity of electricity determined when a point source of LED came on. This design illustrated in Fig. 1 is a direct balance between volume of water and pressure of the steam produced. Excess charges were stored in a 220 μ f, 25 V capacitor of model D 993 VENT, 105 $^{\circ}$ C(m) type. The effect of different variables such as rainfall, time of the day, altitude, proximity of mirror array to boiler were considerable on the

intensity of the LED. The experimental set-up simulated in MATLAB is as shown in Fig. 2. The data referred to as STEG was imputed and different operations were carried out on the values to estimate the time plot, spectra and frequency functions.

3. Results and discussion

The preprocess was necessary to feed the data stock into the MATLAB

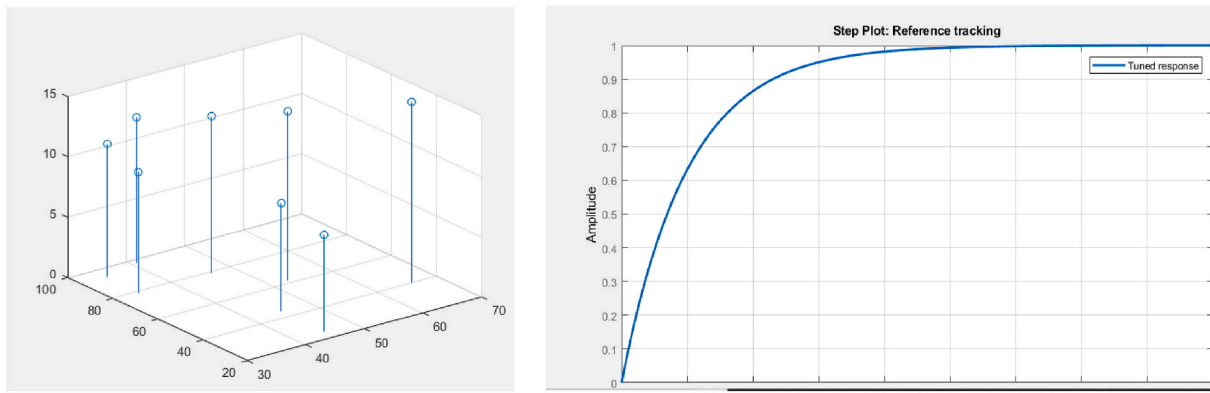


Fig. 11. (a) Spikes depict convective motion and (b) tracking of thermosyphon control of steam.

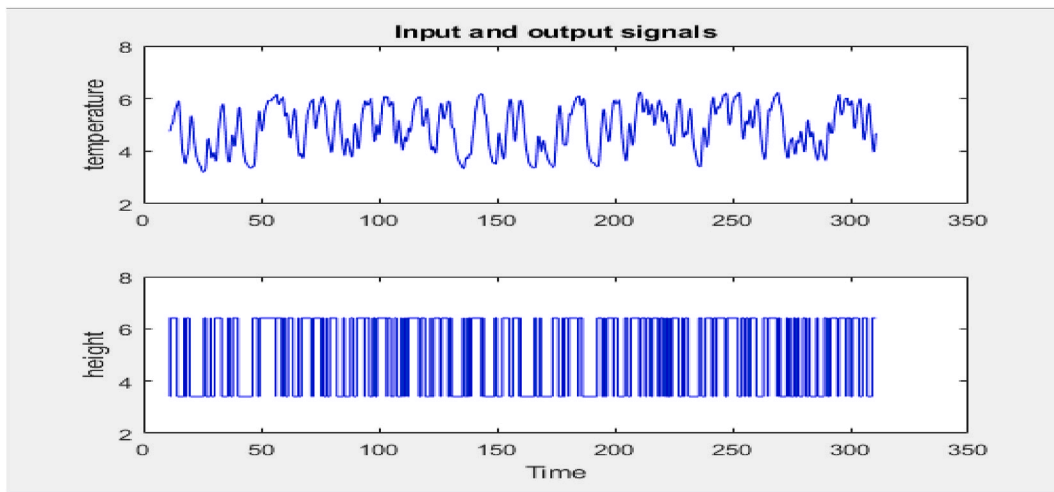


Fig. 12. Aftermath of thermosyphon on steam.

model for STEG, the Process Model Identification with one input (PID1) and Transfer Function with one input (tf1) modelling was used to determine the frequency and transient responses necessary for predictions about the optimal working conditions for the steam thermal energy generator. The result of the experiment is as shown on Tables 1–3. A plot of height of boiler against temperature over time interval was interpolated to determine the relationship and significance of the heating curve.

The electrical and thermal conductivities and Seebeck coefficient of thermo-power are assumed to be constant. Thus, the conversion efficiency is derived from Z (figure of the merit) as shown in Equation (1).

$$Z = \frac{\sigma S^2}{\lambda} \tag{1}$$

where $S = dV/dT$, $Q = 3.14I$ and V , T , Q and I depict voltage, temperature, heat and current respectively.

4. Interpretation of behavior of isotherms and their significance

A suitable interpretation of isothermal lines is crucial to the inclusive upgrading of the STEG adsorption device and pathways. There is no compromising of an effective design independently of the adsorption system. A consideration of the points of congruence (12.10 h, 45 cm, 45 °C), (2.40 h, 58 cm, 58 °C) and (12.20 h, 71 °C) on day 1 Vs day 2 as shown on Table 1 present equilibrium nodes between temperature adsorbed by water in the boiler and relative position in terms of height and distance. In the simplest case, time interval between phases and

interphase changes translate to one-dimensional parameter. Influence of height or distance with time gives the two-dimensional case while height vs distance vs temperature with respect to time provides the three-dimensional basis for this principle. In general terms, this relationship can be illustrated by Equation (2);

$$q_e = K_{HE} C_e \tag{2}$$

where q_e , K_{HE} and C_e connote quantity of steam, Henry’s adsorption constant and equilibrium ratio of steam: concentration of water respectively. In practice, the amount of heat is difficult to access at a particular time hence, we reckon with time intervals. This coincides with 40 min and 3 h 10 min as shown in Fig. 3 (a). Entropy increases (Δs) indicated by increased volume (δV directly indicating a massive phase change. The entire Figure portends to:

$$\Delta q_e = \Delta s = \partial V = K_{HE} \Delta C_e \tag{3}$$

a cyclic process which can be explained by this Equation this increment is attributable to equilibrium of changing phases from water to steam and vice versa [20]. In Fig. 3(b), only a single point of congruence occurs to instigate a switch in distance Vs temperature characteristic atypical of the afore-mentioned phase change.

Investigation of day 2, $\frac{dT}{dt} = \frac{58 \text{ deg.C}}{0.5h}; \frac{85 \text{ deg.C}}{1h}$ reveals higher entropy within the lower and higher peaks as shown in Fig. 4 (a). These are points of potential differences which produced the torque generating electricity illustrated in Fig. 4 (b) as shown. In day 4, this translates to $\frac{65 \text{ deg.C}}{1.15h}; \frac{82 \text{ deg.C}}{1.4h}$ accordingly. Exploring mobile adsorption of heat on the

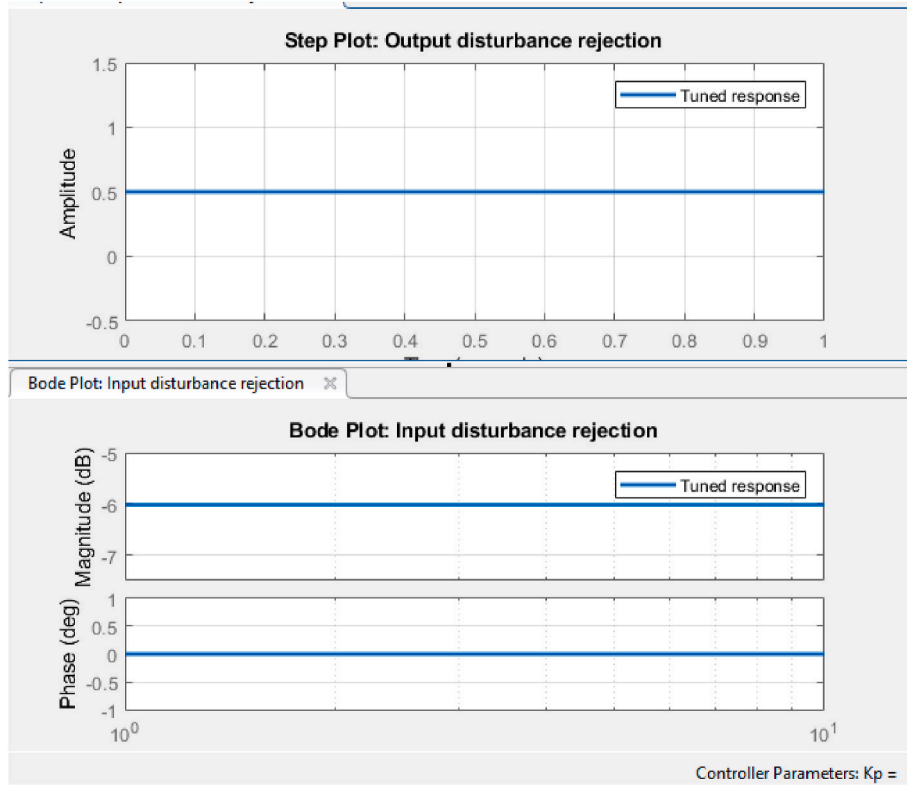


Fig. 13. Bode Analysis of heat exchange in boiler relative to ambient.

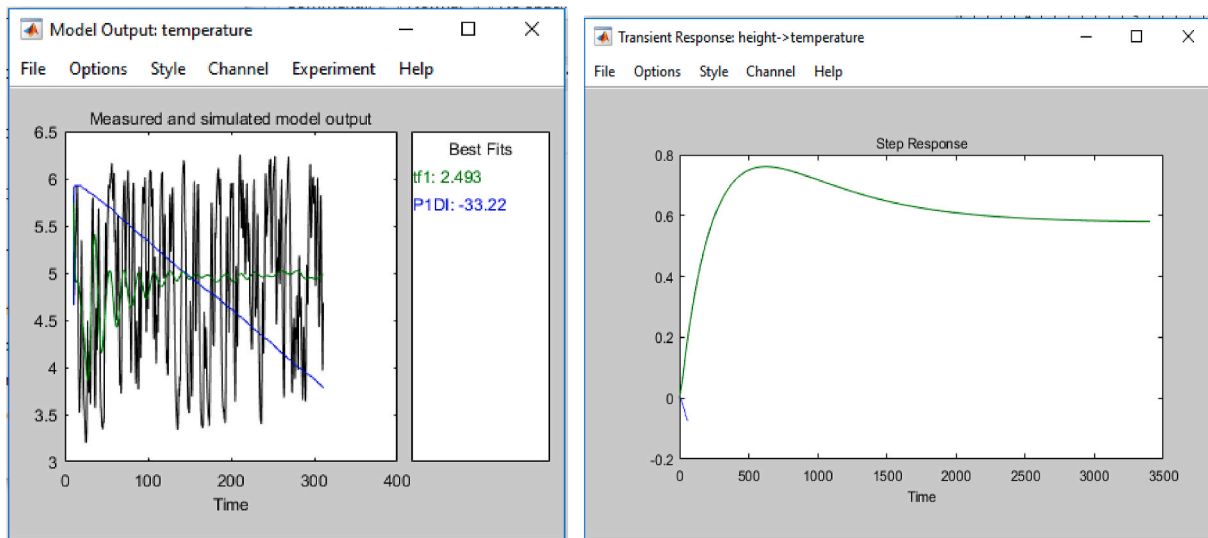


Fig. 14. Hypothetical performance projection of STEG

rotor as well as lateral interaction among adsorbed molecules requires a two-dimensional approach depicted by Equation (4), as shown.

$$\ln \left[\frac{C_e(1-\theta)}{\theta} \right] = -\ln K_{FG} + \frac{2\omega\theta}{RT} \tag{4}$$

where K_{FG} is Fowler-Guggenheim equilibrium constant, θ represents coverage ratio, R is universal constant of gas, T depicts temperature and ω signifies energy of interaction. Thus, $dT/dt = dV/dT = \Delta T = Q = I$ predict the magnitude of the force of interaction. Day 4 > Day 3 > Day 2 > Day 1 > Day 5 > Day 6, as shown in Figs. 4 and 5.

5. Interpretation of behavior of isotherms from software modelling perspective

This model of isotherm is established by data which reveals that, heat of adsorption fluctuates linearly with loading. When interaction between the adsorbed molecules is attractive, the heat of adsorption will intensify with more molecules since degree of interaction between adsorbed molecules increases, this is termed positive. Conversely, if the interaction among adsorbed molecules is repulsive, such as when the heat of adsorption decreases with loading, it is described as negative. But when there is no interaction between adsorbed molecules, the

Fowler-Guggenheim isotherm reduces to the Langmuir equation, which is not applicable in this situation. Interaction of the three isotherms produces sine waveforms which can be analyzed from frequency domain and Fourier's transform as shown in Fig. 6. The general form is given by Equation (5) [22],:

$$x(t) = a \sin(\omega t + \phi) = a \sin(2\pi f t + \phi) \quad (5)$$

substituting f at 40, 50 and 60 dB gives negative value indicating a frequency below the human audible range. This can be related to the imperceptible sound of kinetic energy as water molecules in the boiler change phase to steam, a coarse frequency illustrated in Fig. 7.

6. Applications of isotherms in audio

According to Fourier analysis, possibility of summation of waveforms also creates a possibility of decomposition into component waves. This breakdown is accomplished by obtaining a spectral function of its frequency content. This is represented as Equation (6),

$$E \triangleq \int_{-\infty}^{\infty} |x(t)|^2 dt \quad (6)$$

Equivalent of a discrete-time Fourier transform (DTFT) in energy value, whose combination still produces a frequency too low for the human ear to perceive as illustrated by Fig. 8(a). Breaking the frequency into small time zones results in a periodogram given by Fig. 8(b) which further analyzes the heating process of the boiler.

The rotor represents a heterogenous interface relative to water and steam molecules. A measure of distribution of active regions and energy is described exponentially and pictorially demonstrated earlier in Fig. 8 (b). It shows that the steam builds up with time, increase in temperature leads to phase change, as the steam grows, there is a slight drop in temperature owing to the latent nature of energy required to break the molecular bonds. Normalization is crucial in order to reckon with the forward and inverse Fourier transforms that combined as tri-sinusoidal functions. In this case, time is divided into blocks represented as Equation (7).

$$x_{m(n)} = x(n + mN), n = 0, 1, \dots, N - 1 \quad (7)$$

where m represents the number of blocks.

These shifts are directly linked to change in magnitude and phase angles of the steam from the boiler as indicated in Fig. 9. The significance of neighboring steam atoms molecular interaction in Fig. 9(a), (b) and (c) alter their behavioral frequency. This in turn is responsible for delay in cluster of these molecules, clearly depicted in Fig. 9 (d).

Appendix I

7. Analysis of torque on turbine

Steam serves as a mechanical sensor which contacts the turbine surface to simulate residual stress which causes angular rotation (ω). This is evidenced by the aerial view of Fig. 10, the steam moves vertically, the rotor is positioned horizontally on top. Heat exchange in this setup utilizes scheme of passive exchange of heat, built on ordinary convection process, which mixes a fluid (steam and water) devoid of a powered pump. This thermal management arrangement simplifies heat transfer of the fluid and saves cost and complexity of a conventional pump simulated by Fig. 10. Influence of the thermal management of a thermosiphon is as illustrated in Figs. 11 and 12.

8. Assessment of heat exchanges within the STEG system

The frequency domain behavior is monitored with Bode plots, this is essentially to check indiscriminate heat loss to the surroundings, thereby serving as control and maintaining stability. Tuning the parameters shown by Appendix I and controlling parameters at $K_p = 1$, controlled the thermodynamics and predicts a hypothetical possible time interval of 3500 h with model best fit temperature at 60 °C.

9. Recommendation and conclusion

This work used the thermosiphon principle and Seebeck effect on a black body to achieve a peak temperature of 85°C within 1 h, the conversion efficiency from reference tracking is 0.8. Extending the thermosiphon to encapsulate the entire set-up would incorporate the same conversion efficiency, the phase change at 100°C would yield a sustainable transient response revealed in Figs. 13 and 14. As such, ready application in control and management of engineering and energy systems are areas of immediate spheres of this study. In the reverse, it would work in conjunction with sensors, LEDs, artificial intelligent components in a circuit and cooling and refrigerating systems.

Declaration of competing interest

The authors declare that they have no known competing financial interests or personal relationships that could have appeared to influence the work reported in this paper.

Acknowledgement

The authors wish to appreciate Covenant University for the support of providing the right ambience for the successful completion of this study.

Plant Identification Progress

Process Model Identification

Estimation data: Time domain data STEG
Data has 1 outputs, 1 inputs and 1000 samples.
Model Type:
'FIDI'

Estimation Progress

Achieved improvement: 0.000763953%

Iteration 20:
Current cost: 0.767206 Previous cost: 0.767212

Name	New Value	Previous Value	Direction
Kp:	-0.00146993	-0.00146886	-0.0350962
l/Tpl:	7.92091	7.91331	249.042
Td:	8.1499	8.1504	-16.281
InputOffset:	5.54687	5.54727	-12.8757

Step-size: 0.643259
First-order optimality: 1.24823e+06
Expected improvement: 24.937%

Achieved improvement: 0.000763052%

Estimation complete.
Last improvement: 0.000763052
First-order optimality (largest slope): 1.24823e+06
Final cost: 0.767206

Result

Termination condition: Maximum number of iterations reached.
Number of iterations: 20, Number of function evaluations: 307

Status: Estimated using PROCEST
Fit to estimation data: 1.049%, FFE: 0.680298

Transfer Function Identification
Estimation data: Time domain data STEG
Data has 1 outputs, 1 inputs and 1000 samples.
Number of poles: 8, Number of zeros: 1
Initialization Method: "iv"

Estimation Progress
done.

Initialization complete.

Nonlinear least squares with automatically chosen line search method

Iteration	Cost	Norm of step	First-order optimality	Improvement (%) Expected	Achieved	Bisections
0	52.7667	-	2.17e+07	1.87	-	-
1	16.5221	276	4.48e+08	1.87	68.7	1
2	11.958	48.4	2.44e+08	5.84	27.6	2
3	9.40656	97	1.72e+09	7.97	21.3	3
4	1.35525	21.3	2.62e+09	9.96	85.6	1
5	1.16713	18.5	1.55e+09	41.2	13.9	1
6	1.09854	8.14	2.12e+09	43.1	5.88	3
7	1.06724	6.7	2.58e+09	43.8	2.85	4
8	1.04703	0.00269	3.25e+09	44.3	1.89	4
9	1.03785	0.00594	4.16e+09	44.9	0.877	4
10	1.02472	0.00502	4.65e+09	45.4	1.27	5
11	1.02172	0.000738	4.71e+09	45.6	0.293	8
12	1.02018	0.000375	4.73e+09	45.6	0.151	9

Result

Termination condition: Maximum number of iterations reached.
Number of iterations: 20, Number of function evaluations: 247

Status: Estimated using TFEST
Fit to estimation data: 2.493%, FFE: 0.677999

Controller Parameters	
	Tuned
Kp	0.0001
Ti	1e-05
Td	n/a
N	n/a
b	1
c	n/a

Performance and Robustness	
	Tuned
Rise time	0.22 seconds
Settling time	0.391 seconds
Overshoot	0 %
Peak	1
Gain margin	Inf dB @ NaN rad/s
Phase margin	90 deg @ 10 rad/s
Closed-loop stability	Stable

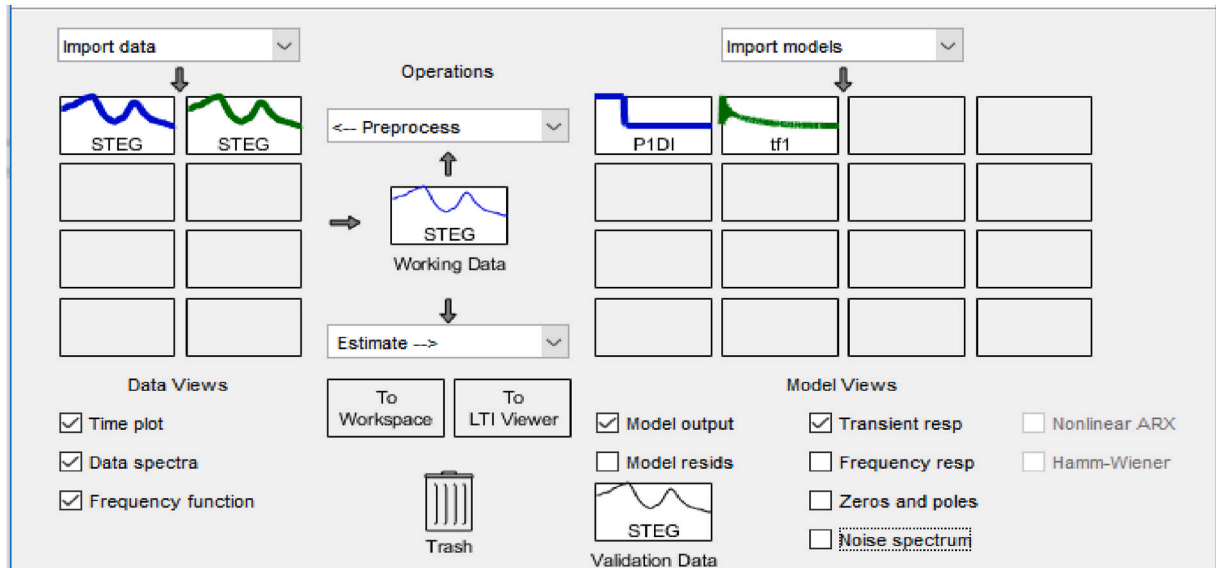
Appendix II

Transfer Function Identification
 Estimation data: Time domain data STEG
 Data has 1 outputs, 1 inputs and 1000 samples.
 Number of poles: 8, Number of zeros: 1
 Initialization Method: "iv"

Estimation Progress						
0	52.7667	-	2.17e+07	1.87	-	-
1	16.5221	276	4.48e+08	1.87	68.7	1
2	11.958	48.4	2.44e+08	5.84	27.6	2
3	9.40656	97	1.72e+09	7.97	21.3	3
4	1.35525	21.3	2.62e+09	9.96	85.6	1
5	1.16713	18.5	1.55e+09	41.2	13.9	1
6	1.09854	8.14	2.12e+09	43.1	5.88	3
7	1.06724	6.7	2.58e+09	43.8	2.85	4
8	1.04703	0.00269	3.25e+09	44.3	1.89	4
9	1.03785	0.00594	4.16e+09	44.9	0.877	4
10	1.02472	0.00502	4.65e+09	45.4	1.27	5
11	1.02172	0.000738	4.71e+09	45.6	0.293	8
12	1.02018	0.000375	4.73e+09	45.6	0.151	9
13	1.01998	4.72e-05	4.74e+09	45.6	0.0194	12
14	1.01997	2.95e-06	4.74e+09	45.6	0.00122	16
15	1.01997	7.38e-07	4.74e+09	45.6	0.000305	18
16	1.01997	1.85e-07	4.74e+09	45.6	7.63e-05	20
17	1.01997	9.23e-08	4.74e+09	45.6	3.81e-05	21
18	1.01997	4.61e-08	4.74e+09	45.6	1.91e-05	22
19	1.01997	1.15e-08	4.74e+09	45.6	4.77e-06	24
20	0.867669	2.55e-05	1.34e+10	45.6	14.9	2

Result
 Termination condition: Maximum number of iterations reached.
 Number of iterations: 20, Number of function evaluations: 247
 Status: Estimated using TFEST
 Fit to estimation data: 2.493%, FPE: 0.677999

Appendix III



MATLAB preprocessing of STEG validation data.

References

[1] K.J. Beatty, J.K. Beatty, C.C. Petersen, A. Chaikin, in: A.A.M. Sayigh (Ed.), *The New Solar System*, Cambridge University Press, 1999 (2012) Solar energy engineering, Elsevier.

[2] (a) A.G.W. Cameron, The formation of the sun and planets, *Icarus* 1 (1–6) (1962) 13–69;
 (b) G. Matijević, T. Zwitter, U. Munari, O. Bienaymé, J. Binney, J. Bland-Hawthorn, G. Gilmore, Double-lined spectroscopic binary stars in the RAVE survey, *Astron. J.* 140 (1) (2010) 184.

- [3] P. Kumar, Generation of electricity from flue gases, *Glob. J. Eng. Sci. Res. Manag.* (2014).
- [4] (a) N.F. Mott, The electrical conductivity of transition metals, *Proc. Roy. Soc. Lond. Math. Phys. Sci.* 153 (880) (1936) 699–717;
(b) G.T. Meaden, *Electrical Resistance of Metals*, Springer, 2013.
- [5] (a) N. Benson, C. Melzer, R. Schmechel, H.V. Seggern, Electronic states at the dielectric/semiconductor interface in organic field effect transistors, *Phys. Status Solidi* 205 (3) (2008) 475–487;
(b) R. Diffenderfer, *Electronic Devices: Systems and Applications*, Cengage Learning, 2005.
- [6] (a) S. Diez, C. Schmidt, R. Ludwig, H.G. Weber, K. Obermann, S. Kindt, K. Petermann, Four-wave mixing in semiconductor optical amplifiers for frequency conversion and fast optical switching, *IEEE J. Sel. Top. Quant. Electron.* 3 (5) (1997) 1131–1145, (b) Ovshinsky, S. R., Johnson, R. R., Cannella, V. D., & Yaniv, Z. (1987). U.S. Patent No. 4,646,266. Washington, DC: U.S. Patent and Trademark Office.
- [7] F. Odobel, L. Le Pleux, Y. Pellegrin, E. Blart, New photovoltaic devices based on the sensitization of p-type semiconductors: challenges and opportunities, *Acc. Chem. Res.* 43 (8) (2010) 1063–1071.
- [8] J.J. Santos, J.C. Palacio, A.M. Reyes, M. Carvalho, A.J. Freire, M.A. Barone, Concentrating solar power, in: *Advances in Renewable Energies and Power Technologies*, Elsevier, 2018, pp. 373–402.
- [9] (a) M. Romero, A. Steinfeld, Concentrating solar thermal power and thermochemical fuels, *Energy Environ. Sci.* 5 (11) (2012) 9234–9245;
(b) W.D. Steinmann, Thermal energy storage systems for concentrating solar power (CSP) technology, in: *Advances in Thermal Energy Storage Systems*, Woodhead Publishing, 2015, pp. 511–531.
- [10] H. Price, E. Lüpfert, D. Kearney, E. Zarza, G. Cohen, R. Gee, R. Mahoney, Advances in parabolic trough solar power technology, *J. Sol. Energy Eng.* 124 (2) (2002) 109–125.
- [11] G.T. Machinda, S. Chowdhury, R. Arscott, S.P. Chowdhury, S. Kibaara, December, Concentrating solar thermal power technologies: a review, in: 2011 Annual IEEE India Conference, IEEE, 2011, pp. 1–6.
- [12] C. Wyman, J. Castle, F. Kreith, A review of collector and energy storage technology for intermediate temperature applications, *Sol. Energy* 24 (6) (1980) 517–540.
- [13] Y. Bhusal, A. Hassanzadeh, L. Jiang, R. Winston, Technical and economic analysis of a novel low-cost concentrated medium-temperature solar collector, *Renew. Energy* 146 (2020) 968–985.
- [14] Y. Bhusal, A. Hassanzadeh, L. Jiang, R. Winston, Technical and economic analysis of a novel low-cost concentrated medium-temperature solar collector, *Renew. Energy* 146 (2020) 968–985.
- [15] P. Horta, T. Osório, M. Collares-Pereira, Energy cost-based design optimization method for medium temperature CPC collectors, in: *AIP Conference Proceedings*, vol. 1734, AIP Publishing LLC, 2016, May, p. 20011. No. 1.
- [16] Diogo Canavarro, et al., New second-stage concentrators (XX SMS) for parabolic primaries; Comparison with conventional parabolic trough concentrators, *Sol. Energy* 92 (2013) 98–105.
- [17] B. Bierman, C. Treynor, J. O'donnell, M. Lawrence, M. Chandra, A. Farver, W. Lindsay, Performance of an enclosed trough EOR system in South Oman, *Energy Proc.* 49 (2014) 1269–1278.
- [18] D. Mills, Advances in solar thermal electricity technology, *Sol. Energy* 76 (2004).
- [19] L. Jame, J.R. Kumar, S.P. Jeyashree, M. Moorthy, Experimental investigation of thermoelectric power generator using D-mannitol phase change material for transient heat recovery, *ECS J. Solid State Sci. Technol.* 10 (2021), 061005.
- [20] A high tech cooling solution, *Pigment Resin Technol.* 36 (3) (2007), <https://doi.org/10.1108/prt.2007.12936cad.005>.
- [21] S. Meir, C. Stephanos, T.H. Geballe, J. Mannhart, Highly-efficient thermoelectronic conversion of solar energy and heat into electric power, *J. Renew. Sustain. Energy* 5 (4) (2013), 043127, <https://doi.org/10.1063/1.4817730>.
- [22] Wanghui Xu, Huanxi Zheng, Yuan Liu, Xiaofeng Zhou, Chao Zhang, Yuxin Song, Xu Deng, Michael Leung, Zhengbao Yang, Ronald X. Xu, Zhong Lin Wang, Xiao Cheng Zeng, Zuankai Wang, A droplet-based electricity generator with high instantaneous power density, *Nature* (2020), <https://doi.org/10.1038/s41586-020-1985-6>.
- [23] Natsumi Komatsu, Yota Ichinose, Oliver S. Dewey, Lauren W. Taylor, Mitchell A. Trafford, Yohei Yomogida, Geoff Wehmeyer, Matteo Pasquali, Kazuhiro Yanagi, Junichiro Kono, Macroscopic weavable fibers of carbon nanotubes with giant thermoelectric power factor, *Nat. Commun.* 12 (1) (2021), <https://doi.org/10.1038/s41467-021-25208-z>.